Available online at www.sciencedirect.com
ScienceDirect
Comput. Methods Appl. Mech. Engrg. 399 (2022) 115339
Computer methods in applied mechanics and engineering
www.elsevier.com/locate/cma

Analysis of dynamic crack propagation in two-dimensional elastic bodies by coupling the boundary element method and the bond-based peridynamics

Yang Yang*, Yijun Liu

Department of Aerospace and Mechanical Engineering, Southern University of Science and Technology, Shenzhen, China

Received 9 February 2022; received in revised form 24 May 2022; accepted 2 July 2022
Available online 28 July 2022

Abstract

A novel method for predicting dynamic crack propagation based on coupling the boundary element method (BEM) and bond-based peridynamics (BBPD) is developed in this work. The special feature of this method is that it can take full advantages of both the BEM and PD to achieve a higher level of accuracy and efficiency. Based on the scale of the structure and the location of cracks, the considered domain can be divided into a non-cracked region and a cracked region. For the non-cracked region, a meshfree boundary-domain integral equation method (meshfree-BDIEM) is employed in the analysis to reduce the dimension by one and to increase the computational efficiency. The bond-based PD is applied to simulate the cracked region, which can model the initiation and propagation of the cracks automatically. The boundary nodes from the BEM on the interfaces can interact with the material points from the PD directly. By using the displacement continuity and force equilibrium conditions on the interfaces, a combined model is obtained by merging the mass, stiffness, and force matrices from each region of the domain. Both the implicit and explicit BEM-PD coupled solution methods can deliver accurate results without inducing the ghost forces. Several benchmark problems of dynamic crack propagation have been modeled by using the method, which demonstrate that the developed BEM-PD coupled approach can be an efficient numerical tool to model the dynamic crack propagation problems.

Keywords: Dynamic crack propagation; Peridynamics; Boundary element method; Implicit and explicit methods; Coupling BEM with PD

1. Introduction

Analysis of dynamic cracks and their growth is an important issue as to avoid catastrophic failures of structures under dynamic loadings. However, dynamic crack problems, such as prediction of the initiation and propagation of cracks in solids, still represent a challenge for the classical continuum mechanics. This is because of the conflict between the continuity hypothesis in the continuum theory and the discontinuity in the actual problem to be solved [1]. Thus, more appropriate theories should be developed to match the discontinuous nature of the crack problems.

* Corresponding author.
E-mail addresses: yangy33@sustech.edu.cn (Y. Yang), liuyj3@sustech.edu.cn (Y. Liu).

https://doi.org/10.1016/j.cma.2022.115339
0045-7825/

Peridynamics (PD) [2] based on non-local theory has been proposed as a particle method in modeling crack problems, where the solid is discretized using a set of material points, and the interactions between these points are expressed in an integral form. Hence, the continuity assumption is not required and the discontinuities such as fractures are captured inherently. Recently, some success has been achieved in applying PD to study the crack propagation problems [3,4], and the PD theory itself has also been improved accordingly [5].

PD introduces the concept of structural damage for material points. However, PD, based on the non-local characteristic, depends on integration of many material points, which renders it a time-consuming numerical method. In order to increase the efficiency, various types of coupling schemes of the PD method with other computational methods were developed [6–8], especially, much effort has been devoted to coupling the PD grids to the FEM meshes for different applications. Macek and Silling [9] proposed to embed PD nodes in FEM elements over a region by displacement constraint. Coupling between PD and FEM was presented by [10], The coupling was introduced by defining an overlap region. The displacement and body force densities in the overlap region were determined using FEM and PD, respectively. Liu and Hong [11] coupled the PD with FEM by introducing the interface elements. The PD method was coupled with classical continuum mechanics using a morphing approach, in which the PD zone is discretized utilizing a discontinuous Galerkin approach [12,13]. An effective way to couple FEM meshes and PD grids was proposed by Galvanetto et al. [14–16] to solve the static and dynamic problems. An implicit coupling FEM and PD was developed [17] for the dynamic problems of solid mechanics with crack propagation. The coupling domain is achieved by considering that the nodes and material points share the common information. Bie et al. [18] proposed the coupling approach of ordinary state-based PD with node-based smoothed FEM. The transient information was governed by the unified coupling equations of motion. An approach was presented by Sun et al. [19] to couple the PD theory with numerical substructure method for modeling structures with local discontinuities. The PD was integrated in the substructure model using interface elements with embedded PD nodes. Even with the above-mentioned approaches, FEM-PD coupling is still an active research area, because most of the coupling methods are affected by some kind of arbitrariness or new approximations [16].

As the name implies, the boundary element method (BEM) requires meshing only on the domain boundary. Thus, it reduces the dimensionality of the problem by one. Based on the analytical fundamental solutions, BEM can achieve improved accuracy, especially for modeling stress concentration problems, such as cracks and their propagations [20,21]. Besides, the computational efficiency of the BEM has been improved significantly with the development of the fast solution methods in the last two decades [22,23].

Therefore, exploring the advantages of coupling the BEM and PD can provide an opportunity for the development of a novel method of modeling crack propagations [24]. The static crack propagation analysis has been carried out by using a coupling approach of the BEM and PD [24]. The numerical examples solved by using this method show a higher computational efficiency than using the approach of the PD coupled with FEM [24]. Thus, the development of a convenient and efficient coupling scheme of the PD and BEM to combine the advantages of these two methods will be of great interests for the dynamic crack propagation problems as well.

In this paper, a coupled BEM and PD is developed to investigate the dynamic crack propagation problems. Different from the coupling approaches mentioned above, the BBPD subregion is directly coupled with the BEM subregion instead of using overlapping regions or the morphing strategy. The continuous displacements and the equilibrium forces are transformed by the interface elements. The dynamic equation with the mass and stiffness matrices for the whole domain is constructed. Both explicit and implicit time integration techniques are employed to investigate the stability and accuracy of the coupled solution method.

The remainder of this paper is outlined as follows: In Section 2, the formulations of bond-based peridynamics and the meshfree boundary-domain integral equation method are reviewed. In Section 3, the coupling method between the BBPD and BEM is described in detail. In Section 4, several numerical examples are studied to verify the proposed coupling approach. Some concluding remarks are made in the final section.

2. BEM and PD formulations

2.1. Review of the BBPD formulation

In the present work, the crack and potential cracked region are modeled by using the PD. Only the BBPD is considered in this present work. A brief outline of the BBPD is presented below, and more details can be found in Ref. [1].

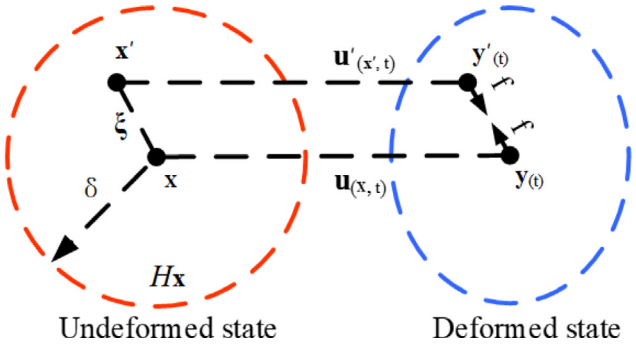

Fig. 1. Description of bond-based PD theory.

The fundamental equation of motion for any material point in BBPD is given by:

$$\rho\ddot{\mathbf{u}}\left(\mathbf{x},t\right)=\int_{H_{\mathrm{x}}}\mathbf{f}\left[\boldsymbol{\eta},\boldsymbol{\xi},t\right]dV_{\mathbf{x}'}+\mathbf{b}\left(\mathbf{x},t\right),\ \forall\mathbf{x}'\in H_{\mathrm{x}} \tag{1}$$

where H_{X} is the neighborhood of point $\mathbf{x}$, which is usually taken to be a spherical region of radius δ centered at point $\mathbf{x}$, as shown in Fig. 1; $\ddot{\mathbf{u}}$ and ρ are the acceleration vector and mass density, respectively, which are the same as in the continuum mechanics; $\mathbf{b}$ is the body force density vector. The response function $\mathbf{f}$, defined as a force vector per unit volume square, represents the response of point $\mathbf{x}'$ when the force is exerted on point $\mathbf{x}$. The initial relative position vector $\boldsymbol{\xi}$ between $\mathbf{x}$ and $\mathbf{x}'$ in the reference configuration and their current relative displacement vector $\boldsymbol{\eta}$ at time t are given, respectively, by

$$\boldsymbol{\xi}=\mathbf{x}'-\mathbf{x}\ \text{and}\ \boldsymbol{\eta}=\mathbf{u}'\left(\mathbf{x}',t\right)-\mathbf{u}\left(\mathbf{x},t\right) \tag{2}$$

For a prototype micro-elastic brittle (PMB) material, the force function $\mathbf{f}$ can be expressed as [25]

$$\mathbf{f}\left(\boldsymbol{\eta},\boldsymbol{\xi}\right)=\frac{\partial w\left(\boldsymbol{\eta},\boldsymbol{\xi}\right)}{\partial\boldsymbol{\eta}}=\frac{\boldsymbol{\eta}+\boldsymbol{\xi}}{|\boldsymbol{\eta}+\boldsymbol{\xi}|}s\left(\boldsymbol{\eta},\boldsymbol{\xi}\right)c\left(\boldsymbol{\xi},\delta\right),\ \forall\boldsymbol{\eta},\boldsymbol{\xi} \tag{3}$$

where $w\left(\boldsymbol{\eta},\boldsymbol{\xi}\right)=\frac{c(\boldsymbol{\xi},\delta)s(\boldsymbol{\eta},\boldsymbol{\xi})^2|\boldsymbol{\xi}|}{2}$ [26] is the micro-elastic potential, $|\cdot|$ is the Euclidean norm. s represents the stretch of a bond, which is related to the strain in continuum mechanics and is expressed as

$$s\left(\boldsymbol{\eta},\boldsymbol{\xi}\right)=\frac{|\boldsymbol{\eta}+\boldsymbol{\xi}|-|\boldsymbol{\xi}|}{|\boldsymbol{\xi}|} \tag{4}$$

Using Taylor's series expansion [24], we can evaluate s as follows:

$$s\left(\boldsymbol{\eta},\boldsymbol{\xi}\right)=\frac{\boldsymbol{\eta}+\boldsymbol{\xi}}{|\boldsymbol{\eta}+\boldsymbol{\xi}|}\cdot\frac{\boldsymbol{\eta}}{|\boldsymbol{\xi}|} \tag{5}$$

Substituting of Eqs. (5) and (2) into Eq. (3), the pairwise force yields,

$$\mathbf{f}\left(\boldsymbol{\eta},\boldsymbol{\xi}\right)=\begin{cases}\frac{c(\boldsymbol{\xi},\delta)}{|\boldsymbol{\xi}|}\left(\mathbf{u}'\left(\mathbf{x}',\mathbf{t}\right)-\mathbf{u}\left(\mathbf{x},\mathbf{t}\right)\right), & |\boldsymbol{\xi}|\leq\delta\\ 0, & |\boldsymbol{\xi}|>\delta\end{cases} \tag{6}$$

where $c\left(\boldsymbol{\xi},\delta\right)=c\left(0,\delta\right)g\left(\boldsymbol{\xi},\delta\right)$ is the micro-modulus function indicating the stiffness of a pairwise bond. The micro-modulus $c\left(0,\delta\right)$ is obtained based on the consistency between the strain energy densities using the PD theory and classical continuum theory. The kernel function $g\left(\boldsymbol{\xi},\delta\right)$ describes the intensity spatial distribution of long-rang forces in the material. A modified micro-modulus function expression proposed by [27] is used in this analysis (Eq. (7)). The variation of the micro-modulus function is plotted in Fig. 2. It not only satisfies the non-local nature of the PD theory precisely, but also reflects the weakening of the long-range force intensity when the distance

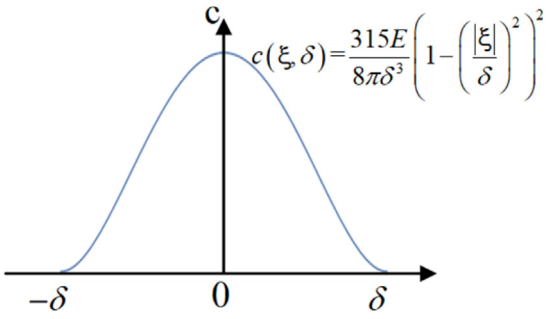

Fig. 2. Variation of the micro-modulus function.

between two particles increases. This leads the PD model to be more localized and thus reduces the quadrature error and the surface effect.

$$c\left(0,\delta\right)=\begin{cases}\frac{72E}{\pi\delta^4}, & \text{3D}\\ \frac{315E}{8\pi\delta^3}, & \text{plane stress}\\ \frac{210E}{5\pi\delta^3}, & \text{plane strain}\end{cases}\quad\text{and, } g\left(\boldsymbol{\xi},\delta\right)=\begin{cases}\left(1-\left(\frac{|\boldsymbol{\xi}|}{\delta}\right)^2\right)^2, & |\boldsymbol{\xi}|\le\delta\\ 0, & |\boldsymbol{\xi}|>\delta\end{cases} \tag{7}$$

where E is the macroscopic Young's modulus. Failure of the material occurs when the stretch s reaches its critical value [27,28]:

$$s_0=\sqrt{\frac{1024\pi G_0}{7\left(120\pi-133\right)E\delta}} \tag{8}$$

where G_0 is the critical energy release rate for mode I fracture.

A bond-breaking parameter $\mu\left(\boldsymbol{\xi},t\right)$ is defined as:

$$\mu\left(\boldsymbol{\xi},t\right)=\begin{cases}1, \text{ if } s<s_0, \text{ for all } 0\le t\\ 0, \text{ otherwise}\end{cases} \tag{9}$$

The rupture of the bond is irreversible so that the constitutive model is history-dependent. The damage level φ at a material point $\mathbf{x}$ at time t is defined as:

$$\varphi\left(\mathbf{x},t\right)=1-\frac{\int_{H_{\mathbf{x}}}\mu\left(\boldsymbol{\xi},t\right)dV_{\mathbf{X}'}}{\int_{H_{\mathbf{x}}}dV_{\mathbf{X}'}},\ 0\le\varphi\le1 \tag{10}$$

It should be noted that $\varphi=0$ represents the undamaged state and $\varphi=1$ is the complete separation of the single material point from all surrounding points within its horizon.

The numerical approximation of the PD equation starts with the subdivision of the structure into nodes, and each node is associated with a certain volume V_j, and the union of all volumes covers the entire body volume. Therefore, the discretized form of Eq. (1) is:

$$\rho\ddot{\mathbf{u}}\left(\mathbf{x}_i,t\right)=\sum_j\mathbf{f}\left(\boldsymbol{\eta},\boldsymbol{\xi},t\right)\upsilon_jV_j\mu\left(\left|\boldsymbol{\xi}_{ij}\right|,t\right)+\mathbf{b}\left(\mathbf{x}_i,t\right),\ \forall\mathbf{x}_j\in H_{\mathbf{x}_i} \tag{11}$$

In the discretized implementation, a regular grid of nodes is used. The grid spacing is the same in all directions ($\Delta x=\Delta y=\Delta z$). Then a cubic cell of volume $V_i=\Delta x^3$ (or a square cell of volume $V_i=\Delta x^2$) is associated to each node which is placed at the center of the corresponding cell. The spatial integration is performed by making use of one integration point. Substituting the pairwise force defined in Eq. (6) yields,

$$\rho\ddot{\mathbf{u}}_i^t+\sum_j\frac{c\left(\boldsymbol{\xi}_{ij},\delta\right)}{\left|\boldsymbol{\xi}_{ij}\right|}\left(\mathbf{u}_i^t-\mathbf{u}_j^t\right)\upsilon_jV_j\mu\left(\left|\boldsymbol{\xi}_{ij}\right|,t\right)=\mathbf{b}_i^t,\ \forall\mathbf{x}_j\in H_{\mathbf{x}_i} \tag{12}$$

where υ_j is the volume reduction factor. When the volume V_j of node j falls completely within the horizon of the central node $\mathbf{x}_i$, υ_j is equal to 1; and when $\delta - \Delta x/2 < \left|\boldsymbol{\xi}_{ij}\right| < \delta$, $\upsilon_j = \left(\delta + \Delta x/2 - \left|\boldsymbol{\xi}_{ij}\right|\right)/\Delta x$. In this paper, a linearized bond-based PD is adopted, since the examples are characterized by small strains and displacements.

The discretized form of Eq. (12) can also be written in a standard matrix form of dynamic system equations as follows:

$$\boldsymbol{\rho}_P \ddot{\mathbf{u}}_P + \mathbf{K}_P \mathbf{u}_P = \mathbf{b}_P \tag{13}$$

Subscript P denotes that the variables are associated with the PD region.

2.2. Formulation of meshfree BDIEM equations

The remaining domain of the elastic body will be modeled by the boundary element method. Due to the fact that the fundamental solutions for the traditional dynamic boundary integral equations are more complicated, a meshfree boundary domain integral equation method [29] is applied based on using the elastostatic fundamental solution. The detailed formulations are presented below.

The governing equations of motion for a 2D homogeneous elastic body occupying domain Ω with boundary Γ is

$$\sigma_{ij,j} + f_i = \rho \ddot{u}_i \tag{14}$$

In Eq. (14), the tensor σ_{ij} and vector u_i are the stress and displacement components, respectively. The stress is related to the displacement field by $\sigma_{ij} = c_{ijkl} u_{k,l}$, where the elastic tensor $c_{ijkl} = \lambda \delta_{ij} \delta_{kl} + G\left(\delta_{ik}\delta_{jl} + \delta_{il}\delta_{jk}\right)$, and $\lambda = E\upsilon/(1+\upsilon)(1-2\upsilon)$, shear modulus $G = E/2(1+\upsilon)$, υ is the Poisson's ratio, and δ_{ij} is the Kronecker symbol.

Assuming the body force $f_i = 0$, and applying the Somigliana's identity for elastostatic problems and the Gauss's divergence theorem, the displacement integral equation can be obtained as [22]:

$$\begin{aligned} c_i(\mathbf{x})\, u_i(\mathbf{x}, t) = & \int_\Gamma U_{ij}^*(\mathbf{x}, \mathbf{y})\, t_j(\mathbf{y}, t)\, d\Gamma(\mathbf{y}) - \int_\Gamma T_{ij}^*(\mathbf{x}, \mathbf{y})\, u_j(\mathbf{y}, t)\, d\Gamma(\mathbf{y}) \\ & - \int_\Omega \rho U_{ij}^*(\mathbf{x}, \mathbf{y})\, \ddot{u}_j(\mathbf{y}, t)\, d\Gamma(\mathbf{y}) \end{aligned} \tag{15}$$

where c_i is a constant coefficient, $t_j = \sigma_{jk} n_k$ is the traction, U_{ij}^* and T_{ij}^* are the elastostatic fundamental solutions for the displacement and traction, respectively. For the 2D plane strain case [22]:

$$\begin{cases} U_{ij}^*(\mathbf{x}, \mathbf{y}) = \frac{1}{8\pi(1-\upsilon)G}\left[(3-4\upsilon)\,\delta_{ij} \ln\left(\frac{1}{r}\right) + r_{,i} r_{,j}\right] \\ T_{ij}^*(\mathbf{x}, \mathbf{y}) = \frac{-1}{4\pi(1-\upsilon)r}\left\{(1-2\upsilon)\left(n_i r_{,j} - n_j r_{,i}\right) + \left[(1-2\upsilon)\,\delta_{ij} + 2r_{,i} r_{,j}\right] r_{,l} n_l\right\} \end{cases} \tag{16}$$

in which $r = |\mathbf{x} - \mathbf{y}|$ is the distance between the source point $\mathbf{x}$ and the field point $\mathbf{y}$; n_j is the component of the outward unit normal n to the boundary Γ of the considered domain Ω.

It should be noted that a domain integral exists in the displacement integral Eq. (15), due to the employed static fundamental solutions for the dynamic equation. In order to maintain the advantage of BEM in discretizing the domain with boundary elements only, this domain integral will be transformed into the boundary integral by using the radial integration method [30]. First, the acceleration in the domain integral is expressed by a combination of the radial basis function and polynomials as:

$$\begin{cases} \ddot{u}_j(\mathbf{y}, t) = \sum_A \ddot{\alpha}_j^A(t)\, \phi^A(R) + \ddot{a}_j^k(t)\, y_k + \ddot{a}_j^0(t) \\ \sum_A \ddot{\alpha}_i^A = 0 \\ \sum_A \ddot{\alpha}_i^A y_j^A = 0 \end{cases} \tag{17}$$

where $\ddot{\alpha}_j^A(t)$, $\ddot{a}_j^k(t)$ and $\ddot{a}_j^0(t)$ are the parameters to be determined; y_k and y_j^A are the coordinates of the field point $\mathbf{y}$ and the application point A respectively. The collocation scale of A will directly affect the efficiency and accuracy of the radial integration, and which always composed by the boundary nodes and some integral nodes as depicted in Fig. 3(a). For the sake of description in the following equations, the boundary nodes, internal and application points are denoted as *'b'*,*'i'* and *'t'*. $\phi^A(R)$ is the 4th order spline radial basis function as shown below, which has

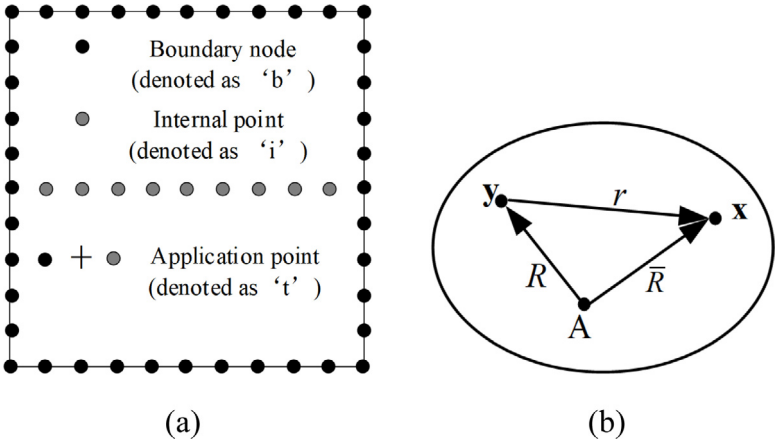

Fig. 3. (a) The collocation points in BEM domain; (b) the relationships of the source point, field point and application point.

been verified as the most efficient radial basis functions [29,30]:

$$\phi^A(R) = \begin{cases} 1 - 6\left(\frac{R}{d_A}\right)^2 + 8\left(\frac{R}{d_A}\right)^3 - 3\left(\frac{R}{d_A}\right)^4, 0 \le R < d_A \\ 0, \qquad\qquad R \ge d_A \end{cases} \tag{18}$$

where R is the distance between field point $\mathbf{y}$ and the application point A, and d_A is the collocation scale of application points. The relationships between the source point, field point and application point are plotted in Fig. 3(b).

Using Eq. (17) and the radial integration technique, the domain integral can be written as:

$$\begin{cases} \int_\Omega \rho \ddot{u}_j U_{ij}^* d\Omega = \rho\left(\sum_A \ddot{\alpha}_j^A \int_\Gamma \frac{1}{r}\frac{\partial r}{\partial n} P_{ij}^A d\Gamma + \ddot{a}_j^k \int_\Gamma \frac{1}{r}\frac{\partial r}{\partial n} P_{ij}^k d\Gamma + \ddot{a}_j^0 \int_\Gamma \frac{1}{r}\frac{\partial r}{\partial n} P_{ij}^0 d\Gamma\right) \\ P_{ij}^A = \int_0^r r\phi^A U_{ij}^* dr \\ P_{ij}^k = \int_0^r r y_k U_{ij}^* dr \\ P_{ij}^0 = \int_0^r r U_{ij}^* dr \end{cases} \tag{19}$$

Then, an integral equation with only boundary integrals is obtained and expressed as:

$$\begin{aligned} &c_i u_i = \int_\Gamma U_{ij}^* t_j d\Gamma - \int_\Gamma T_{ij}^* u_j d\Gamma \\ &-\rho\left(\sum_A \ddot{\alpha}_j^A \int_\Gamma \frac{1}{r}\frac{\partial r}{\partial n} P_{ij}^A d\Gamma + \ddot{a}_j^k \int_\Gamma \frac{1}{r}\frac{\partial r}{\partial n} P_{ij}^k d\Gamma + \ddot{a}_j^0 \int_\Gamma \frac{1}{r}\frac{\partial r}{\partial n} P_{ij}^0 d\Gamma\right) \end{aligned} \tag{20}$$

Discretizing the boundary integral equation using quadratic boundary elements [29,30], Eq. (20) can be written in a matrix form as:

$$\mathbf{M}_B\ddot{\mathbf{u}} + \mathbf{K}_B\mathbf{u} = \mathbf{G}_B\mathbf{t} \tag{21}$$

in which the index B denotes the BEM domain. In order to keep a consistent form with PD domain matrix equation, where only the force vector is on the right-hand side of the equation, a series matrix operators are taken as follows. First, the matrices are partitioned according to the boundary nodes ($[M_{bt}]$, $[K_{bt}]$, $[G_{bb}]$) and internal nodes ($[M_{it}]$, $[K_{it}]$, $[G_{ib}]$):

$$\begin{bmatrix} M_{bt} \\ M_{it} \end{bmatrix} \{\ddot{u}_t\} + \begin{bmatrix} K_{bt} \\ K_{it} \end{bmatrix} \{u_t\} = \begin{bmatrix} G_{bb} \\ G_{ib} \end{bmatrix} \{t_b\} \tag{22}$$

Then, inverse of $[G_{bb}]$ is multiplied to the both sides of the first equations in (22). Finally, one obtains the matrix equations as:

$$\begin{bmatrix} \bar{M}_{bt} \\ \bar{M}_{it} \end{bmatrix} \{\ddot{u}_t\} + \begin{bmatrix} \bar{K}_{bt} \\ \bar{K}_{it} \end{bmatrix} \{u_t\} = \begin{Bmatrix} t_b \\ 0 \end{Bmatrix} \tag{23}$$

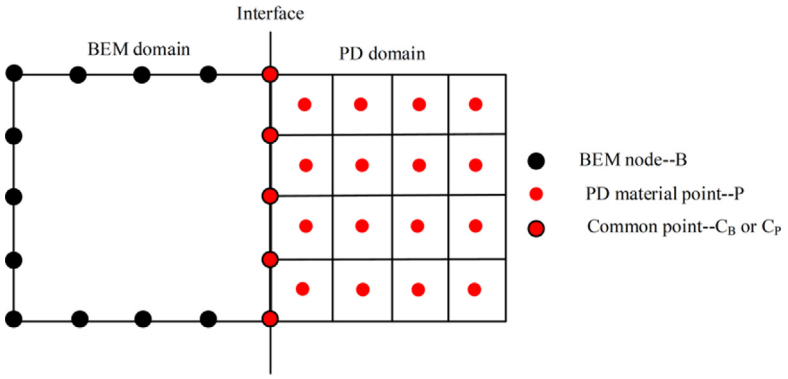

Fig. 4. The coupled scheme of PD and BEM.

where

$$\begin{cases} \bar{M}_{bt} = G_{bb}^{-1} M_{bt} \\ \bar{K}_{bt} = G_{bb}^{-1} K_{bt} \end{cases} \text{and} \quad \begin{cases} \bar{M}_{it} = M_{it} - G_{ib}\left(G_{bb}^{-1} M_{bt}\right) \\ \bar{K}_{it} = K_{it} - G_{ib}\left(G_{bb}^{-1} K_{bt}\right) \end{cases} \tag{24}$$

For large scale problems, the G matrix can be multiplied to the varied force at each time step without computing the inverse.

2.3. The coupled equations

The coupling approach is based on the idea proposed in [24], where the coupled stiffness matrix is defined and used to solve linear static problems. To gain the efficiency from BEM analyses and exploit the generality of PD in the presence of discontinuities, the solution domain is partitioned into a BEM subdomain, where there is no crack, and a PD subdomain, where cracks exist or are expected to propagate, as shown in Fig. 4. Due to the local nature of BEM, the overall computational cost and surface effect can be greatly reduced. In PD domain, each node in the center of a square cell has a uniform mass distribution. The nodes on the interface are boundary nodes in BEM domain, which are also seen as the material points in the PD domain. No gap or overlap into the domain is needed.

The nodes on the BEM domain boundaries are denoted by 'b', the internal nodes are denoted by 'i', and the common nodes on the interfaces are denoted by 'c'. The matrices are constructed as displayed:

$$\begin{bmatrix} \bar{M}_{bb} & \bar{M}_{bc} & \bar{M}_{bi} \\ \bar{M}_{cb} & \bar{M}_{cc} & \bar{M}_{ci} \\ \bar{M}_{ib} & \bar{M}_{ic} & \bar{M}_{ii} \end{bmatrix} \begin{Bmatrix} \ddot{u}_b \\ \ddot{u}_{bc} \\ \ddot{u}_i \end{Bmatrix} + \begin{bmatrix} \bar{K}_{bb} & \bar{K}_{bc} & \bar{K}_{bi} \\ \bar{K}_{cb} & \bar{K}_{cc} & \bar{K}_{ci} \\ \bar{K}_{ib} & \bar{K}_{ic} & \bar{K}_{ii} \end{bmatrix} \begin{Bmatrix} u_b \\ u_{bc} \\ u_i \end{Bmatrix} = \begin{Bmatrix} t_b \\ t_{bc} \\ 0 \end{Bmatrix} \tag{25}$$

The PD equation is also constituted by the common nodes on the interfaces and other internal material points, and is presented as:

$$\begin{bmatrix} \rho_c & 0 \\ 0 & \rho_p \end{bmatrix} \begin{Bmatrix} \ddot{u}_{pc} \\ \ddot{u}_p \end{Bmatrix} + \begin{bmatrix} K_{cc} & K_{cp} \\ K_{pc} & K_{pp} \end{bmatrix} \begin{Bmatrix} u_{pc} \\ u_p \end{Bmatrix} = \begin{Bmatrix} b_{pc} \\ b_p \end{Bmatrix} \tag{26}$$

The common nodes on the interfaces should satisfy the displacements continuity and the traction equilibrium. A transformation operation can be used to construct the equilibrium relationship between the traction in BEM domain and the body force in PD domain, and is described as (see Fig. 5):

$$\begin{cases} u_{bc} = u_{pc} = u_c \\ t_{bc} = -b_{pc} \cdot \Delta x \end{cases} \tag{27}$$

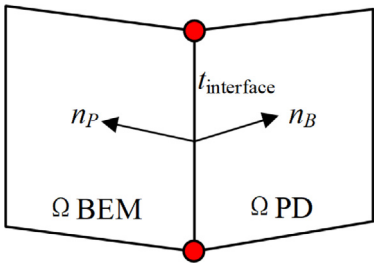

Fig. 5. Traction equilibrium of interface nodes.

Thus, based on Eq. (27), the BEM and PD equations can be coupled as follows:

$$\begin{bmatrix} \bar{M}_{bb} & \bar{M}_{bc} & \bar{M}_{bi} & 0 \\ \bar{M}_{cb} & \bar{M}_{cc}+\rho_c\cdot\Delta x & \bar{M}_{ci} & 0 \\ \bar{M}_{ib} & \bar{M}_{ic} & \bar{M}_{ii} & 0 \\ 0 & 0 & 0 & \rho_p \end{bmatrix} \begin{Bmatrix} \ddot{u}_b \\ \ddot{u}_c \\ \ddot{u}_i \\ \ddot{u}_p \end{Bmatrix} + \begin{bmatrix} \bar{K}_{bb} & \bar{K}_{bc} & \bar{K}_{bi} & 0 \\ \bar{K}_{cb} & \bar{K}_{cc}+K_{cc}\cdot\Delta x & \bar{K}_{ci} & K_{cp}\cdot\Delta x \\ \bar{K}_{ib} & \bar{K}_{ic} & \bar{K}_{ii} & 0 \\ 0 & K_{pc} & 0 & K_{pp} \end{bmatrix} \begin{Bmatrix} u_b \\ u_c \\ u_i \\ u_p \end{Bmatrix} = \begin{Bmatrix} t_b \\ 0 \\ 0 \\ b_p \end{Bmatrix} \tag{28}$$

or

$$\mathbf{M\ddot{u}} + \mathbf{Ku} = \mathbf{F} \tag{29}$$

As verified from several examples, only the number of boundary nodes on the interface and its parallel edges require the same density in distribution as that of the PD grid, while other boundary nodes and internal nodes have no special size requirement.

2.4. Time integration techniques

In order to better solve the dynamic equation, Eq. (29), two explicit and three implicit time integration algorithms have been implemented and compared in terms of their efficiency. Two explicit direct integration methods are the central difference scheme and one which is based on the Velocity-Verlet scheme. Three implicit time integral methods are Houbolt, Newmark and the Wilson-θ. The proposed coupling method work properly with all the integration schemes. The details of each scheme are reported below:

Central difference method (CDM):

$$\begin{cases} \ddot{u}^t = \left(u^{t-\Delta t} - 2u^t + u^{t+\Delta t}\right)/\Delta t^2 \\ \dot{u}^t = \left(u^{t+\Delta t} - u^{t-\Delta t}\right)/2\Delta t \end{cases} \tag{30}$$

where $u^{t-\Delta t} = u^t - \Delta t\dot{u}^t + \frac{\Delta t^2}{2}\ddot{u}^t$ and $\Delta t < \sqrt{\frac{2\rho}{\sum_j V_j c_j}}$

with equivalent equation as:

$$\left(\frac{\mathbf{M}}{\Delta t^2}\right) u^{t+\Delta t} = \mathbf{F}^t - \left(\mathbf{K} - \frac{2\mathbf{M}}{\Delta t^2}\right) u^t - \left(\frac{\mathbf{M}}{\Delta t^2}\right) u^{t-\Delta t} \tag{31}$$

where V_j and c_j represent the occupied volume of node j and the corresponding micro-modulus. Equivalent stiffness and force matrices are $\mathbf{K}^* = \frac{\mathbf{M}}{\Delta t^2}$ and $\mathbf{F}^* = \mathbf{F}^t - \left(\mathbf{K} - \frac{2\mathbf{M}}{\Delta t^2}\right) u^t - \left(\frac{\mathbf{M}}{\Delta t^2}\right) u^{t-\Delta t}$, respectively.

Velocity-Verlet method (V-V):

$$\begin{cases} \dot{u}^{t+\frac{1}{2}\Delta t} = \dot{u}^{t} + \frac{\Delta t}{2}\ddot{u}^{t} \\ u^{t+\Delta t} = u^{t} + \Delta t \dot{u}^{t+\frac{1}{2}\Delta t} \\ \dot{u}^{t+\Delta t} = \dot{u}^{t+\frac{1}{2}\Delta t} + \frac{\Delta t}{2}\ddot{u}^{t+\Delta t} \end{cases} \quad \text{where } \Delta t = \frac{\Delta_{\min}}{\sqrt{\frac{E}{3(1-2\nu)\rho}}} \tag{32}$$

with equivalent equation as:

$$\left(\frac{2\mathbf{M}}{\Delta t^2}\right)\dot{u}^{t+\Delta t} = \mathbf{F}^{t+\Delta t} + \left(\mathbf{M} - \frac{\mathbf{K}\Delta t^2}{2}\right)\ddot{u}^{t} + \left(\frac{2\mathbf{M}}{\Delta t} - \mathbf{K}\Delta t\right)\dot{u}^{t} - \mathbf{K}u^{t} \tag{33}$$

where $\Delta_{\min}$ is the length of the shortest bond in the grid (the minimum nodal distance in the discretized domain). Equivalent stiffness and force matrices are $\mathbf{K}^{*} = \frac{2\mathbf{M}}{\Delta t^2}$ and $\mathbf{F}^{*} = \mathbf{F}^{t+\Delta t} + \left(\mathbf{M} - \frac{\mathbf{K}\Delta t^2}{2}\right)\ddot{u}^{t} + \left(\frac{2\mathbf{M}}{\Delta t} - \mathbf{K}\Delta t\right)\dot{u}^{t} - \mathbf{K}u^{t}$, respectively.

The Houbolt method:

$$\begin{cases} \ddot{u}^{t+\Delta t} = \left(2u^{t+\Delta t} - 5u^{t} + 4u^{t-\Delta t} - u^{t-2\Delta t}\right)/\Delta t^2 \\ \dot{u}^{t+\Delta t} = \left(11u^{t+\Delta t} - 18u^{t} + 9u^{t-\Delta t} - 2u^{t-2\Delta t}\right)/6\Delta t \end{cases} \tag{34}$$

with equivalent equation as:

$$\left(\frac{2\mathbf{M}}{\Delta t^2} + \mathbf{K}\right)u^{t+\Delta t} = \mathbf{F}^{t+\Delta t} + \left(\frac{5\mathbf{M}}{\Delta t^2}\right)u^{t} - \left(\frac{4\mathbf{M}}{\Delta t^2}\right)u^{t-\Delta t} + \left(\frac{\mathbf{M}}{\Delta t^2}\right)u^{t-2\Delta t} \tag{35}$$

which are two-backward-difference formulas. It is more accurate to calculate $u^{t-\Delta t}$ and $u^{t-2\Delta t}$ by some other means. Equivalent stiffness and force matrices are $\mathbf{K}^{*} = \frac{2\mathbf{M}}{\Delta t^2}$ and $\mathbf{F}^{*} = \mathbf{F}^{t+\Delta t} + \left(\frac{5\mathbf{M}}{\Delta t^2}\right)u^{t} - \left(\frac{4\mathbf{M}}{\Delta t^2}\right)u^{t-\Delta t} + \left(\frac{\mathbf{M}}{\Delta t^2}\right)u^{t-2\Delta t}$, respectively.

The Newmark method:

$$\begin{cases} \dot{u}^{t+\Delta t} = \dot{u}^{t} + \left[(1-\delta)\ddot{u}^{t} + \delta\ddot{u}^{t+\Delta t}\right]\Delta t \\ u^{t+\Delta t} = u^{t} + \dot{u}^{t}\Delta t + \left[\left(\frac{1}{2} - \alpha\right)\ddot{u}^{t} + \alpha\ddot{u}^{t+\Delta t}\right]\Delta t^2 \end{cases} \tag{36}$$

with equivalent equation as:

$$\left(\frac{\mathbf{M}}{\alpha\Delta t^2} + \mathbf{K}\right)u^{t+\Delta t} = \mathbf{F}^{t+\Delta t} + \left(\frac{\mathbf{M}}{\alpha\Delta t^2}\right)u^{t} + \left(\frac{\mathbf{M}}{\alpha\Delta t}\right)\dot{u}^{t} + \left[\left(\frac{1}{2\alpha} - 1\right)\mathbf{M}\right]\ddot{u}^{t} \tag{37}$$

where α and δ, which control the integration accuracy and stability, are parameters to be determined. Newmark was originally proposed as an unconditionally stable scheme. It is a constant-average-acceleration method (also called trapezoidal rule) when $\delta = 1/2$ and $\alpha = 1/4$. However, a modified Newmark method [29] with $\delta = 0.7$ and $\alpha = 0.5$ are used in this analysis. Equivalent stiffness and force matrices are $\mathbf{K}^{*} = \frac{\mathbf{M}}{\alpha\Delta t^2} + \mathbf{K}$ and $\mathbf{F}^{*} = \mathbf{F}^{t+\Delta t} + \left(\frac{\mathbf{M}}{\alpha\Delta t^2}\right)u^{t} + \left(\frac{\mathbf{M}}{\alpha\Delta t}\right)\dot{u}^{t} + \left[\left(\frac{1}{2\alpha} - 1\right)\mathbf{M}\right]\ddot{u}^{t}$, respectively.

The Wilson-θ method:

$$\begin{cases} \ddot{u}^{t+\Delta t} = \frac{6}{\theta^3\Delta t^2}\left(u^{t+\theta\Delta t} - u^{t}\right) - \frac{6}{\theta^2\Delta t}\dot{u}^{t} + \left(1 - \frac{3}{\theta}\right)\ddot{u}^{t} \\ \dot{u}^{t+\Delta t} = \dot{u}^{t} + \left[\ddot{u}^{t} + \ddot{u}^{t+\Delta t}\right]\frac{\Delta t}{2} \end{cases} \tag{38}$$

with equivalent equation as:

$$\left(\frac{6\mathbf{M}}{\theta^2\Delta t^2} + \mathbf{K}\right)u^{t+\theta\Delta t} = \mathbf{F}^{t+\theta\Delta t} + \left(\frac{6\mathbf{M}}{\theta^2\Delta t^2}\right)u^{t} + \left(\frac{6\mathbf{M}}{\theta\Delta t}\right)\dot{u}^{t} + (2\mathbf{M})\ddot{u}^{t} \tag{39}$$

For unconditional stability we need to use $\theta \geq 1.37$, and usually we employ $\theta = 1.4$. Equivalent stiffness and force matrices are $\mathbf{K}^{*} = \left(\frac{6\mathbf{M}}{\theta^2\Delta t^2} + \mathbf{K}\right)$ and $\mathbf{F}^{*} = \mathbf{F}^{t+\theta\Delta t} + \left(\frac{6\mathbf{M}}{\theta^2\Delta t^2}\right)u^{t} + \left(\frac{6\mathbf{M}}{\theta\Delta t}\right)\dot{u}^{t} + (2\mathbf{M})\ddot{u}^{t}$, respectively.

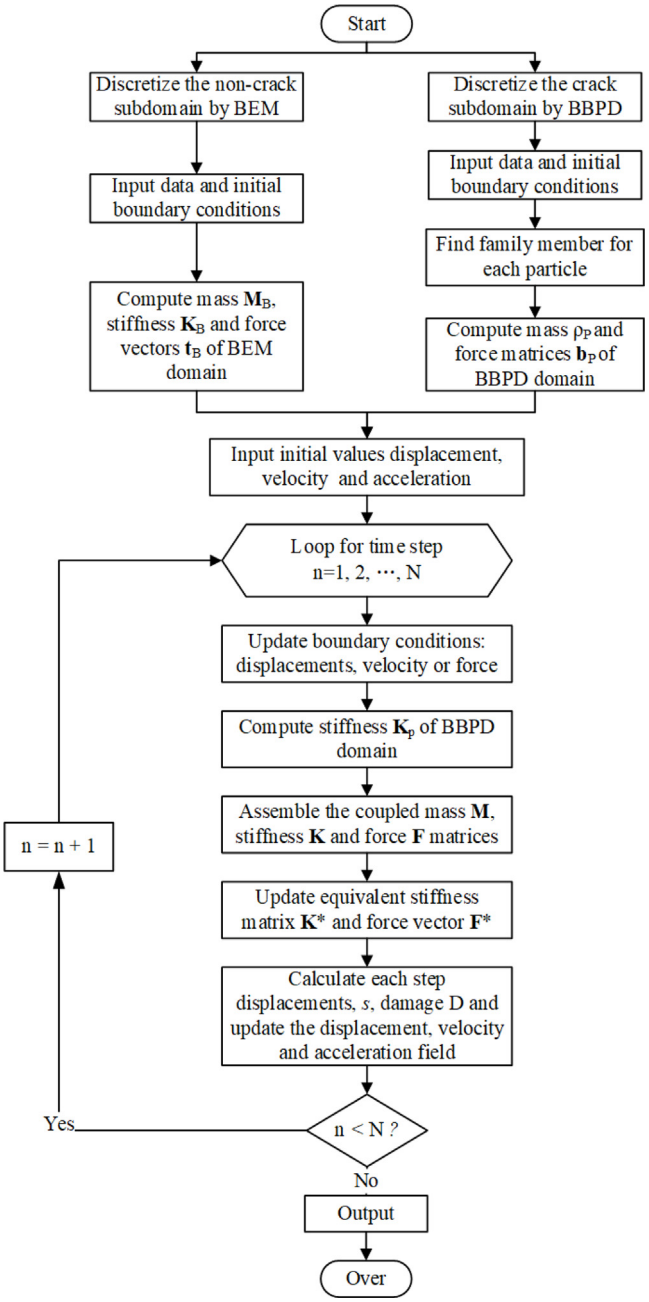

Fig. 6. Flowchart for solving the dynamic problem with the proposed coupled BEM-PD method.

All the time integration approaches satisfy the prescribed initial conditions as follows:

$$\begin{cases} u = u_0 \,\text{at}\, t = 0 \\ \dot{u} = v_0 \,\text{at}\, t = 0 \end{cases} \tag{40}$$

For each time step, the displacements, velocities and accelerations of all nodes can be obtained by solving the equivalent equations. The loop on time steps continues until the final time step. The flowchart for solving the dynamic problem with the proposed coupled BEM-PD method is shown in Fig. 6.

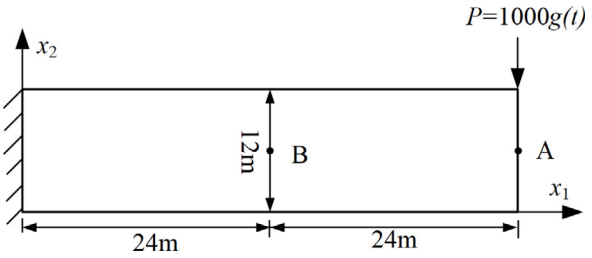

Fig. 7. A plate under a dynamic load.

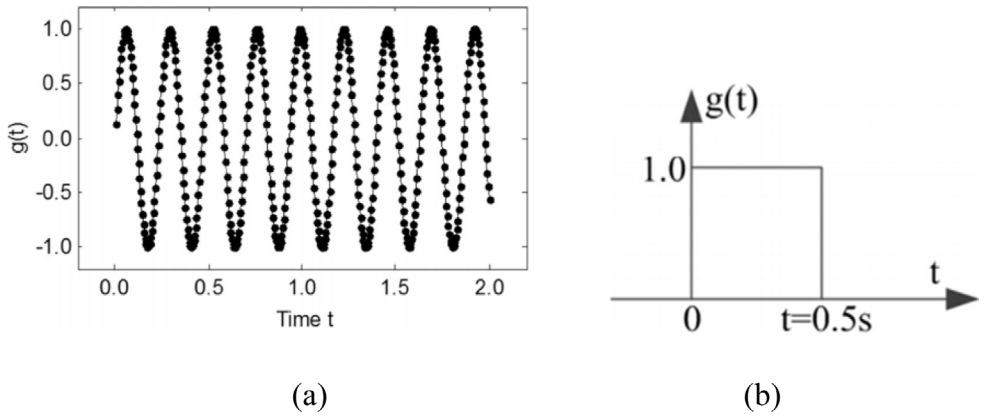

Fig. 8. The dynamic load: (a) a harmonic load, and (b) a transient load.

3. Numerical examples

In this section, the coupled BEM-PD method is applied to analyze some dynamic problems. First, the accuracy and efficiency of the developed method is investigated using a harmonic and transient vibration of a plate. Then, the developed coupled method is applied to model a few dynamic crack propagation problems.

In PD, the ratio $m = \delta/\Delta$ (radius of the horizon to the nodal spacing) plays an important role in the accuracy and quality of numerical solution, especially in the case of failure analysis [7]. A survey of studies [31–33] in the literature reveals that $m \geq 3$ has been adopted for most cases. In the present study $m = 3$ is used.

All the simulations are performed with a research Fortran code and a computer having Intel(R) Xeon(R) Gold 6136 CPU, 128 GB RAM Windows 10 Pro 64 bit OS.

3.1. Efficiency and ghost force test

A plate with 48 m in length and 12 m in width, fixed at the left side and subjected to a in plane dynamic force at the free end (Fig. 7). The parameters used are $E = 3.0 \times 10^7$ Pa, $v = 0.3$ and $\rho = 1.0$ kg/m^3. External excitation force $P = 1000g\,(t)$. For a harmonic load $g\,(t) = \sin(\omega t)$ with frequency $\omega = 27$, and for a transient load $g\,(t) = 1, 0 \leq t \leq 0.5$ s, as shown in Fig. 8.

Two different cases are considered. First, the cantilever is divided into two equal subdomains as plotted in Fig. 9. A total of 16 boundary elements and 9 internal nodes are used to discretize the left BEM subdomain. In the PD domain, nodal spacing is given as $\Delta x = 3$ m, which results in 57 total nodes. It should be noted that the BEM domain edge which is parallel to the interface should have the same nodal interval as the material spacing in PD domain. The solutions obtained by the considered models for the vertical displacement component of the nodes A and B are presented for an interval of 2.0 s.

For comparison, the displacement response of Point A and B calculated by BEM-only [29], PD-only [24] and the present BEM-PD method are shown in Fig. 10 and Fig. 11 for the harmonic and transient load, respectively. In the BEM-only case, the nodal distance is 1.5 m and $dt = 5.0 \times 10^{-3}$ s. In the PD-only case, the nodal spacing

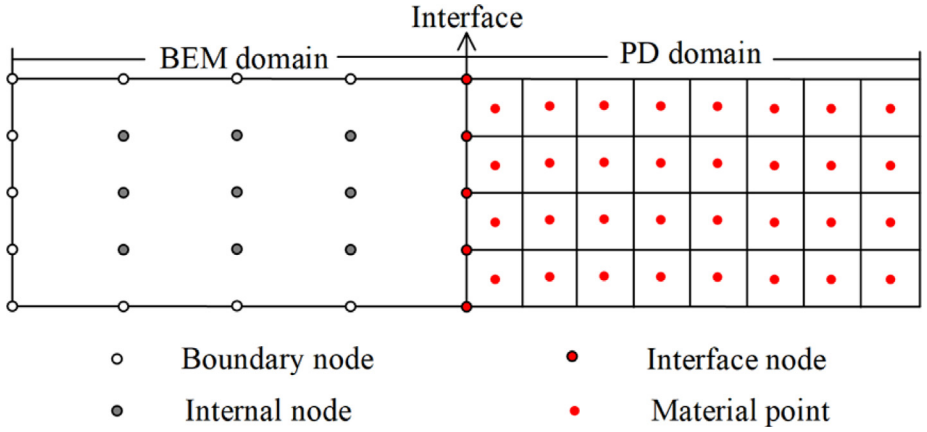

Fig. 9. Discretization of the plate with two subdomains.

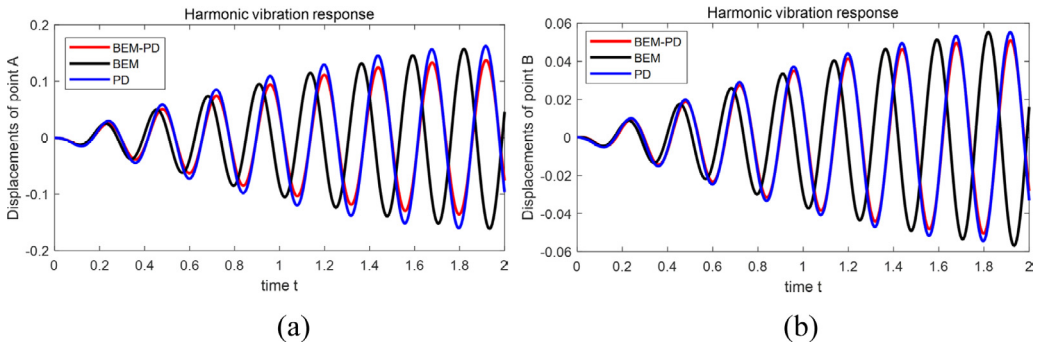

Fig. 10. Comparison of harmonic displacement responses: (a) point A; (b) point B.

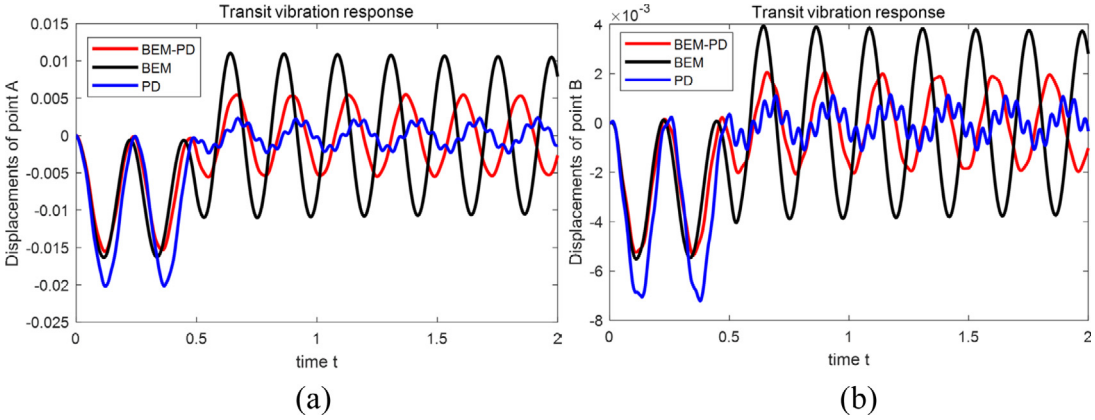

Fig. 11. Comparison of transient displacement responses: (a) point A; (b) point B.

is $\Delta x = 0.4$ m, which is 7.5 times smaller than that of the coupled method, and $dt = 5.0 \times 10^{-4}$ s. It can be seen that as the integration time increases, an increased phase error occurred between the BEM-only and PD-only displacements response. Such a small difference between the solutions is due to the wave dispersion property of PD, and it can be mitigated by refining the solution domain [31]. The results obtained by the BEM-PD coupled method are in agreement with PD solutions.

Table 1
Efficiency scheme comparison for harmonic vibration of the plate.

Methods	Node spacing (m)	Total nodes	Time interval	CPU time (s)
BEM	3.0	61	0.005	500.83
BBPD	0.4	3600	0.0005	13266.78
BEM-PD	3.0	57	0.0002	58.53
Ref. [5]	0.6	1701	0.00012	–

The above-mentioned harmonic vibration of the plate is also studied by Shojaei et al. in Ref. [5], where an averaged nodal spacing of 0.6 m is used with 1701 nodes. Although with almost 30 times the total nodes number of the current coupled BEM-PD method, the results in Ref. [5] have the similar accuracy.

It should be noted that, smaller node spacing will lead the time integration steps to grow significantly and slow down the convergence. The material point spacing in the PD subdomain can be set up with a little larger length according to the BEM scheme to speed up convergence without decreasing the accuracy. For this case, a large node spacing is employed in the BEM-PD method, a smaller time interval is set to illustrate its efficiency. Table 1 shows that, with almost same number of the nodes, the time integral step of BEM-PD is 25 times than that of BEM-only, but it takes one tenth of the time used with the BEM-only. As it known, the BBPD is time consuming, which using 36 times number of points and 200 times seconds obtains the same accuracy of BEM-PD coupled method. Therefore, by comparison, it can be concluded that, the developed BEM-PD coupled method can achieve accurate dynamic results by using a coarser nodal spacing with high efficiency.

To have more insight of the effect of the point collocation, three cases of collocation distribution are investigated as depicted in Fig. 12. The node intervals on the top and bottom edges of the BEM domain remain the same, and the node intervals on the interface and the edges which are parallel to the interface vary with the material point spacing in PD domain. The material spacing for these three cases are $\Delta x = 3$ m, $\Delta x = 1.5$ m and $\Delta x = 1$ m, respectively. The vertical displacements of these three cases, again at points A and B are plotted in Fig. 13. The results of these three cases are almost the same with that of PD-only. With decreasing material point spacing, the amplitude of the displacement response approaches that using PD only.

To explore the efficiency of the time integration techniques, two explicit and three implicit time integral approaches mentioned above are employed to analyze the harmonic and transient vibration of the plate. The displacement responses of point A and B are presented in Figs. 14 and 15, respectively. It can be seen from Fig. 14(a) that the CDM and V-V approaches can yield stable results for the harmonic vibration, but the displacements response at point A has small dissipation error in the high-frequency regime for the transient vibration (Fig. 14(b)). For implicit BEM-PD coupled method, the displacement responses are stable for the harmonic or transient vibration with only small amplitude differences among Houbolt, Newmark and Wilson methods as shown in Fig. 15. Fig. 16 plots the transverse and vertical displacements response contours for the harmonic and transient vibration. It can be concluded that, the variations of the displacements are continuous and smooth and there is no ghost force at the interfaces.

The same plate, which is divided into three equal subdomains, is studied next. The central subdomain is discretized using the PD, and the remaining subdomains are discretized using the BEM. Similarly, the node intervals on the interfaces and the edges parallel to the interfaces need to be the same as the point spacing in the PD domain. The material point spacing is $\Delta x = 2$ m, and the node intervals on the top and bottom edges of the BEM domains can be arranged discretionarily. The discretization scheme is shown in Fig. 17. The explicit and implicit time integration methods are employed to solve the BEM-PD coupled dynamic equations. Straightforward implementation of CMD and V-V, which are explicit time integral approaches, may increase the error and cause divergence. However, with the implicit time integration approaches, stable results can be obtained quickly. The displacement responses of point A for harmonic and transient vibrations by implicit BEM-PD are shown in Fig. 18, and the corresponding displacement contour plots are also shown in Fig. 19, with no ghost force effects.

Numerical error in the displacement field at element interfaces is often the drawback of the various coupling formulations (such as FEM-PD formulations). Compatibility of the displacement field at element interfaces plays a key role in the stability of these formulations. The verification examples demonstrate that the present BEM-PD coupled equations are appropriate for assembling the BEM and PD equations together with no ghost force effects. The dynamic responses show that the use of the implicit time integration can lead to stable results much faster, especially when using the Houbolt and the modified Newmark Method.

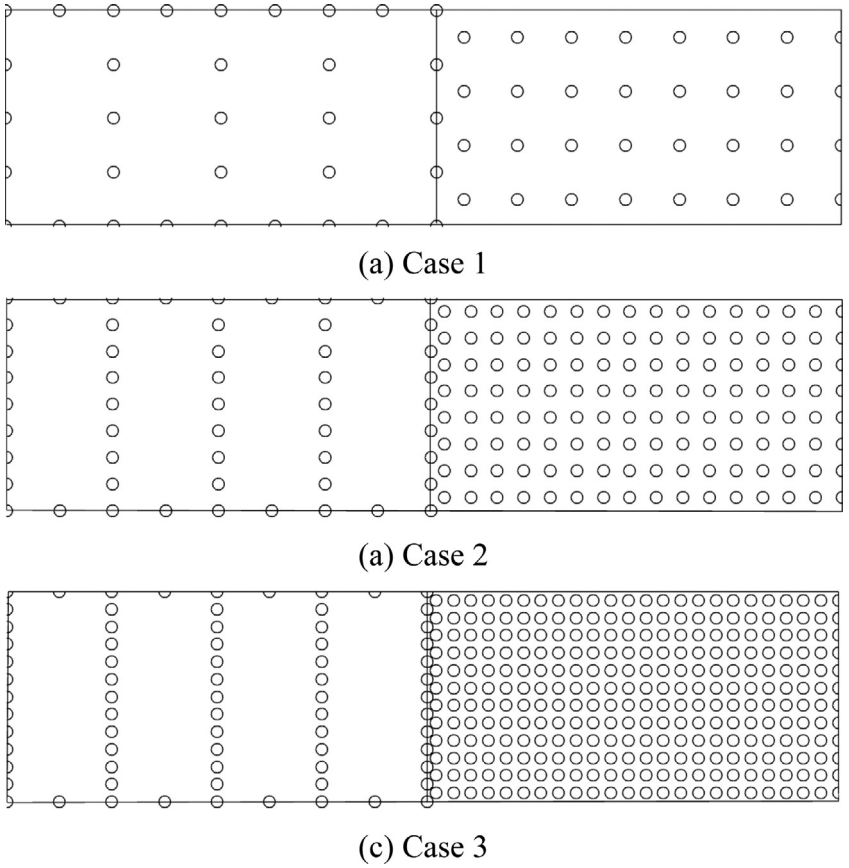

Fig. 12. Three cases of node collocations.

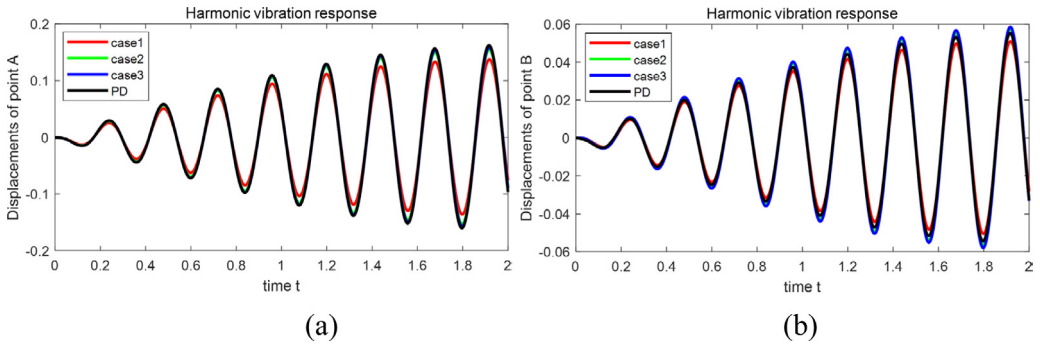

Fig. 13. Displacement responses with three cases of nodes collocation: (a) point A; (b) point B.

3.2. Examples of crack propagation

This part is devoted to show the capability of the present method in solving dynamic crack propagation problems. Two benchmark examples are presented below.

A pre-notched plate

The first example considered is a pre-notched rectangular plate with dimensions 0.1×0.04 m^2, as shown in Fig. 20. The brittle material used is Duran Glass with $E = 65$ GPa, $\rho = 2235$ kg/m^3, and fracture energy $G_0 = 204$ J/m^2. The fracture energy value used in this example is experimentally measured at the branching

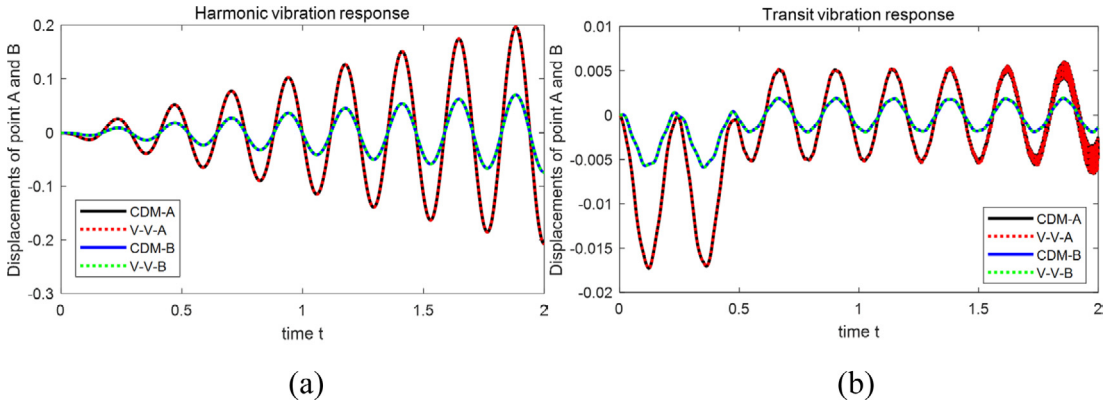

Fig. 14. Displacements response of the explicit BEM-PD coupled method (a) harmonic vibration; (b) transient vibration.

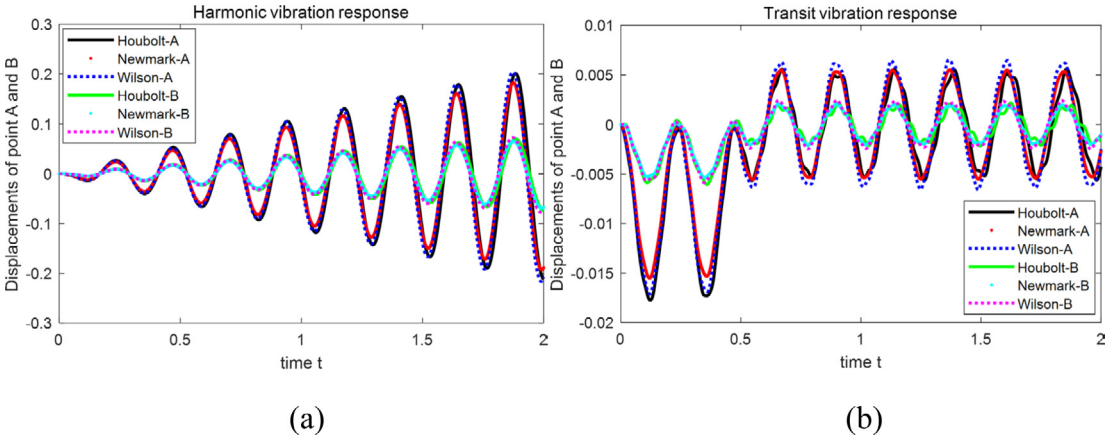

Fig. 15. Displacement responses of the implicit BEM-PD coupled method (a) harmonic response; (b) transient response.

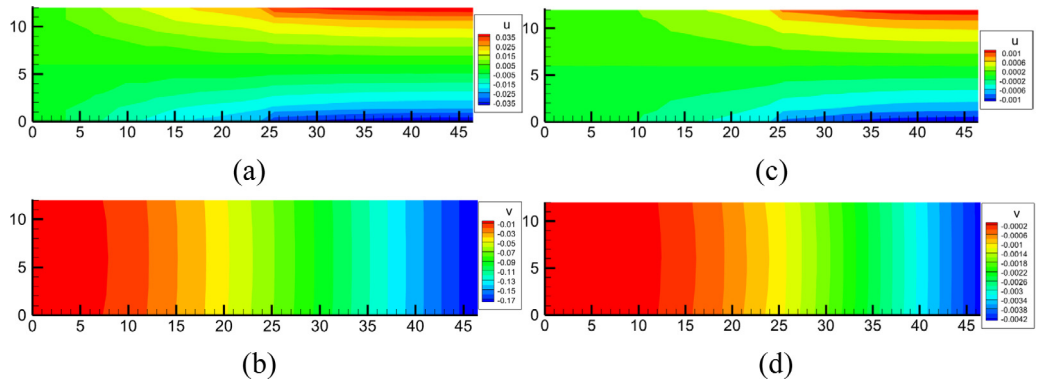

Fig. 16. Displacement contour plots: (a) u of harmonic vibration, (b) v of harmonic vibration, (c) u of transient vibration, (d) v of transient vibration.

for a dynamic crack [7,34]. A tension load $\sigma = 12$ MPa is applied to the upper and lower edges at the initial time step and maintained at the same level after that.

The grid is made of BEM nodes and PD nodes. PD nodes are distributed in the region where the pre-crack is located as well as in the whole region in front of the crack tip where there is the possibility of crack propagation.

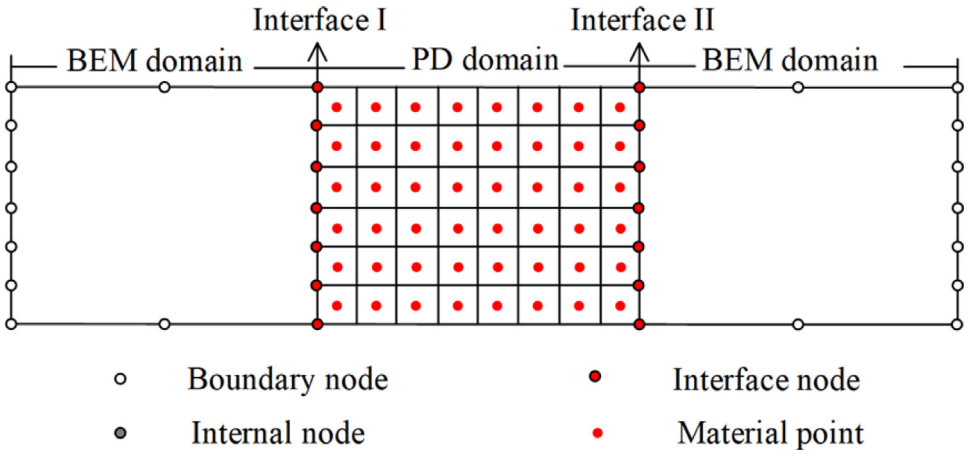

Fig. 17. Discretization of three subdomains.

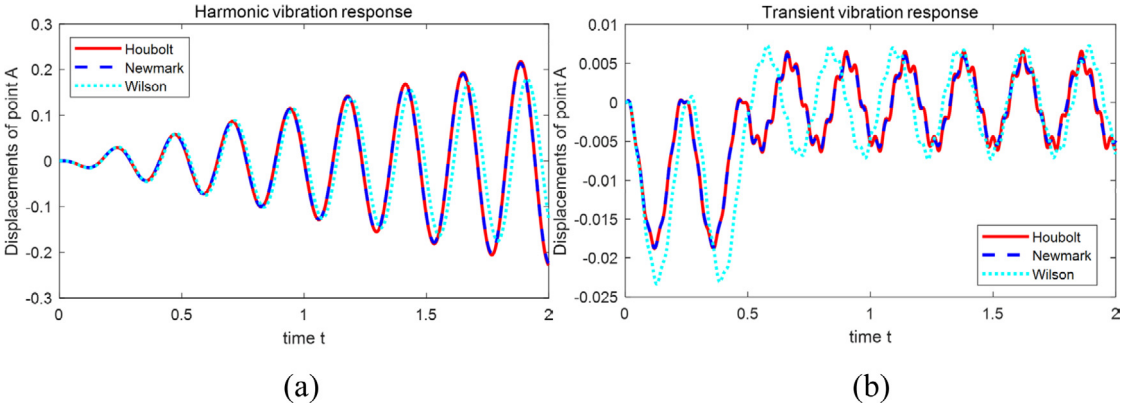

Fig. 18. Displacement responses of point A for (a) harmonic and (b) transient load.

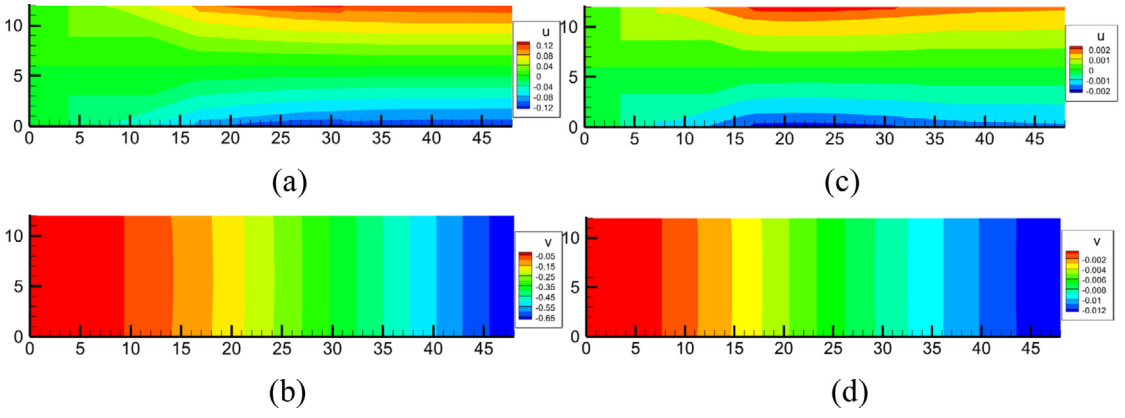

Fig. 19. Displacement response contour plots for (a) u and (b) v for harmonic load; (c) u and (d) v for transient load.

The remaining region of the solution domain is discretized by using BEM nodes. The load is directly applied to the BEM domain, which can eliminate the boundary effect in using the PD. The initial crack is conveniently modeled by breaking the corresponding bonds in PD. In addition, the BEM nodes are positioned far enough from the initial

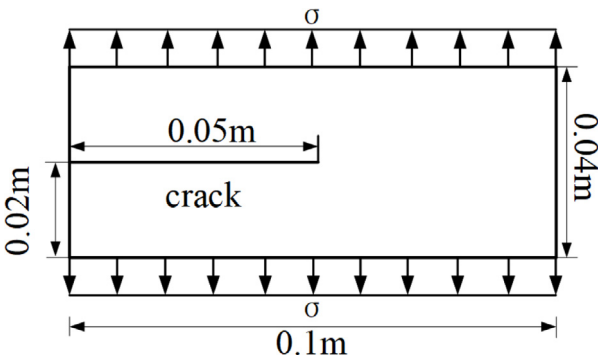

Fig. 20. A pre-notched rectangular plate.

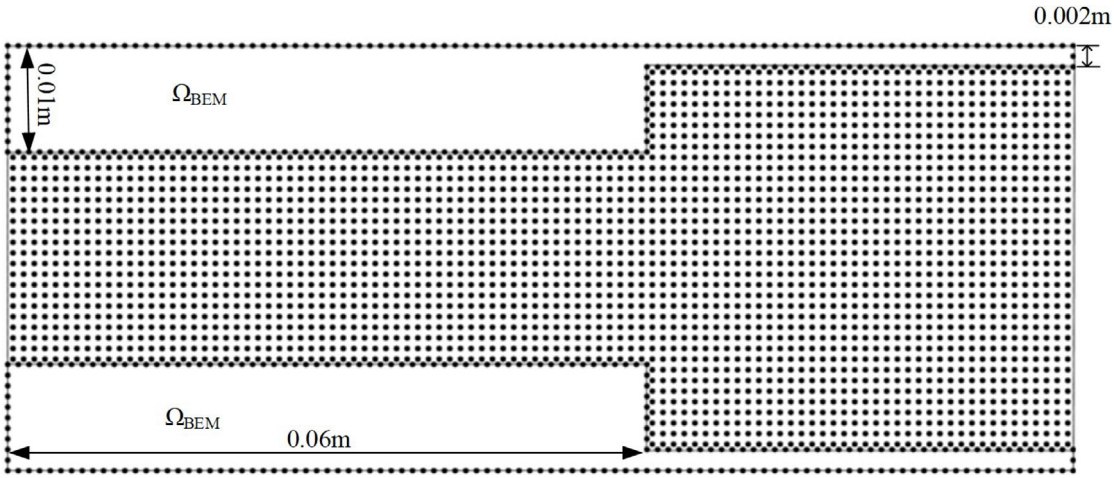

Fig. 21. BEM-PD model of the rectangular plate.

Table 2
Efficiency comparison for traction of pre-cracked plate.

Methods	Node spacing (m)	Total nodes	Time interval	CPU (s)
BBPD	0.001	4000	40 ns	37679.53
BEM-PD	0.001	3080	40 ns	5088.19

crack so that the visibility criterion is observed. For the whole model, a grid with an average nodal spacing of $\Delta x = 0.001$ m with 3080 nodes in total is considered as shown in Fig. 21.

Five plots of damage levels and the corresponding displacement contours at various instants are shown in Fig. 22. The total simulation time is 64 μs with a time step of 40 ns. The crack starts propagating at $n_{step} = 280$ and branches at around $n_{step} = 890$ at $x_{branch} = 0.068$ m measured from the left edge of the plate. The results are in very good agreement with those obtained for a full PD model with $\Delta x = 0.001$ m, where the following values were obtained: $t_{start} = 7$ μs, $t_{branch} = 23.9$ μs and $x_{branch} = 0.0682$ m. The integration time used with the BEM-PD method is almost one seventh of that using the full PD model as listed in Table 2.

Using different values of the applied tensile stress, different crack patterns are observed as shown in Fig. 23. It can be seen that the crack grows along a straight path without any branching and runs through the plate when the tensile stress $\sigma = 0.2$ MPa (Fig. 23(a)). When $\sigma = 12$ MPa, the crack is first seen to propagate along the branch direction, and suddenly the crack begins to split into two stable branches, and subsequently reached the top and bottom edge of the plate (Fig. 23(d)). When the applied tensile stress is increased to $\sigma = 22$ MPa, the crack first branches and then the branches go across the plate in the horizontal direction (Fig. 23(g)).

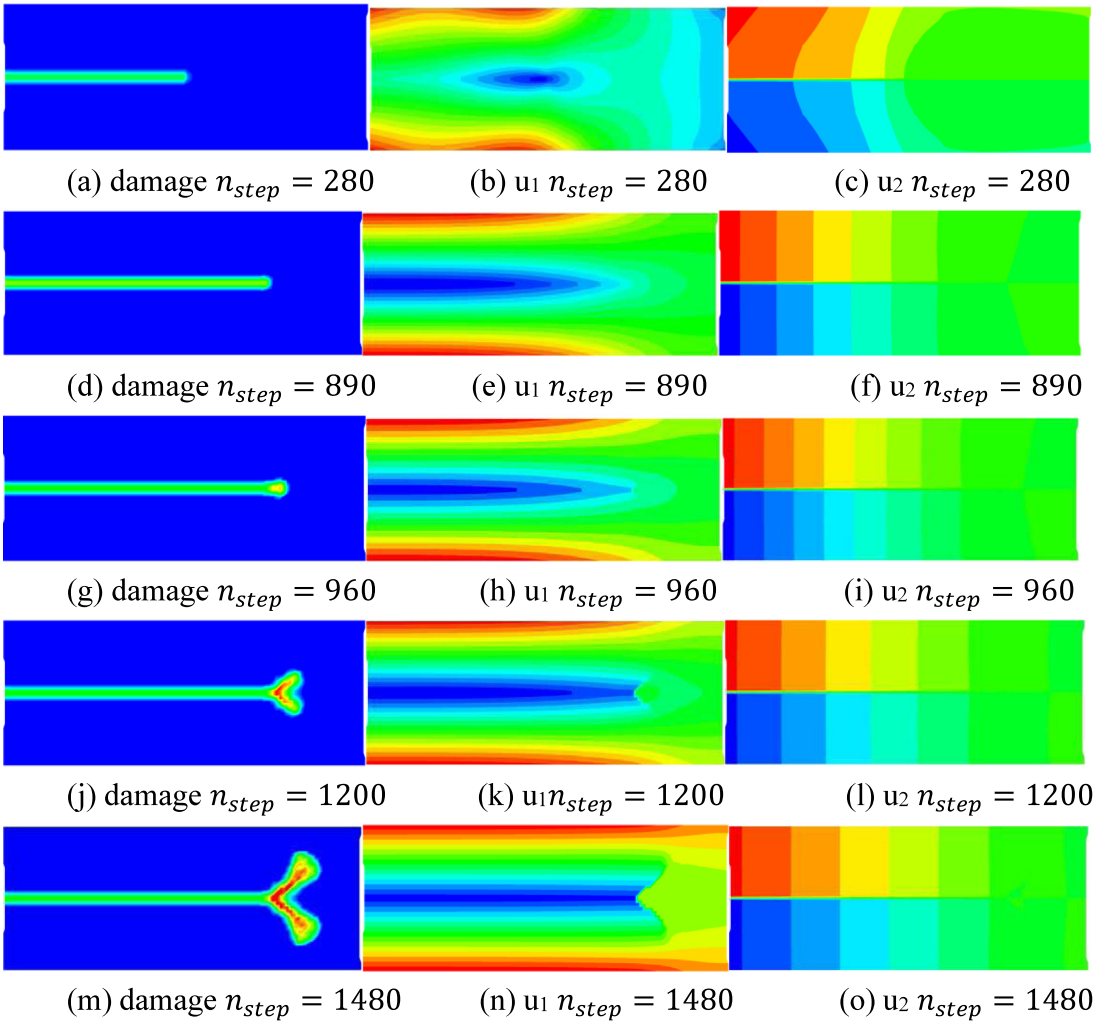

Fig. 22. Contour plots of the crack propagation and displacement.

Kalthoff–Winkler's experiment

Another well-known study of fracture dynamics is the Kalthoff–Winkler's experiment [35], in which a pre-cracked steel plate is hit on the top as shown in Fig. 24. It shows that the fracture type of such experiment configuration depends on the impact speed. When the plate is made of steel 18Ni1900, an impact speed causes a brittle fracture mainly in mode I. The crack propagation takes place at an angle of approximately 70 degrees with respect to the vertical direction.

A BEM-PD coupled model has been established as shown in Fig. 25. On the top, three independent rectangular BEM subdomains with 0.04 m in height are discretized by boundary and internal nodes. Coupled with the BEM subdomains at three interfaces is the PD subdomain, which is 0.06 m in height with two notches. A coarse model with $\Delta x = 0.002$ m is used to discretize the BEM-PD model. The properties of the material are $E = 191$ GPa, $\rho = 8000$ kg/m^3, $G_0 = 42408$ J/m^2 and $\nu = 0.25$ with plane strain conditions assumed. The fracture dynamics is simulated by imposing the impact on the top surface of the sample between the two cracks with an initial vertical speed of $v = 32.0$ m/s. We assume that the projectile and the plate have the same elastic impedance, and boundaries are free. The simulation duration is $t = 117.45$ μs with a time step $\Delta t = 87$ ns is chosen. A full PD model with $\Delta x = 0.0001$ m are also studied for comparison.

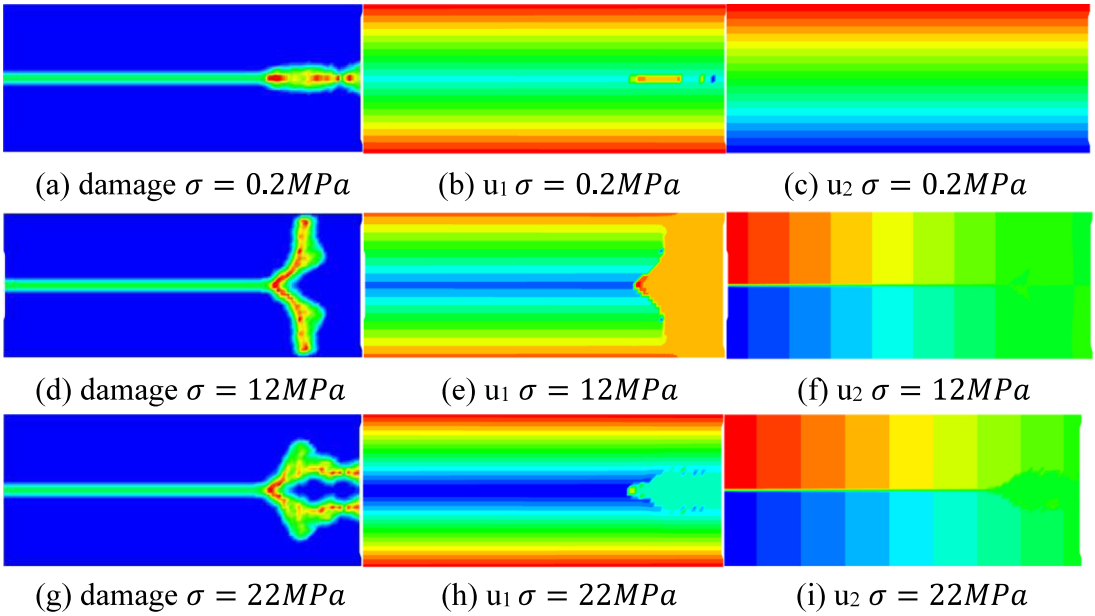

Fig. 23. Crack morphology and corresponding displacement contour plots obtained by applying different tensile stresses.

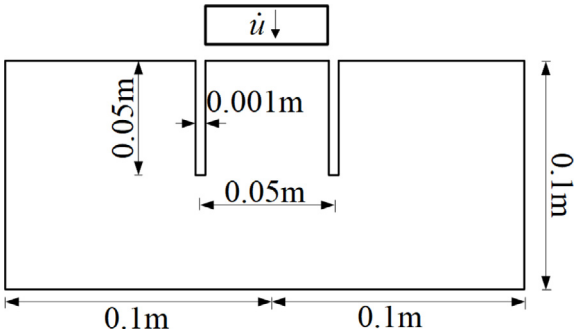

Fig. 24. Model geometry of the Kalthoff–Winkler's example.

Table 3
Comparison of CPU times for the Kalthoff–Winkler's example.

Methods	Node spacing (m)	Total nodes	Time interval	CPU (s)
BBPD	0.0001	20101	87 ns	33266.78
BEM-PD	0.002	3330	87 ns	3350.16

Fig. 26 shows a sequence of frames of the damaged plate. The impact creates compressive stress waves that move into the interior of the plate. As these waves interact with the notch tips, mode-II loading occurs and depending on the impact velocity, fracture may initiate at the notch tips at $t = 25.23$ μs. However, the cracks do not grow in parallel to the notches. Instead, a mode transition occurs, and the notches grow as mode-I cracks along straight lines at 68-degree angles to the notches. This result agrees with the experimentally determined propagation paths. A similar fracture patten was observed in the full PD model and in Ref. [17]. However, the present BEM-PD coupled approach has a much higher computational efficiency than that of the BBPD, as is illustrated in Table 3. The CPU time used with the BEM-PD approach is about one tenth of that with the full PD approach.

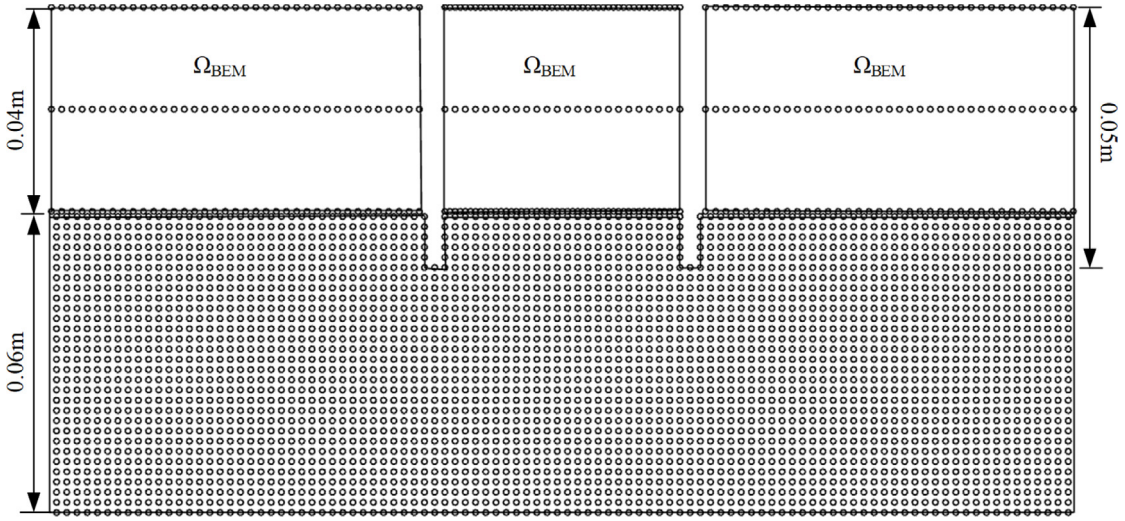

Fig. 25. BEM-PD model of the Kalthoff–Winkler's example.

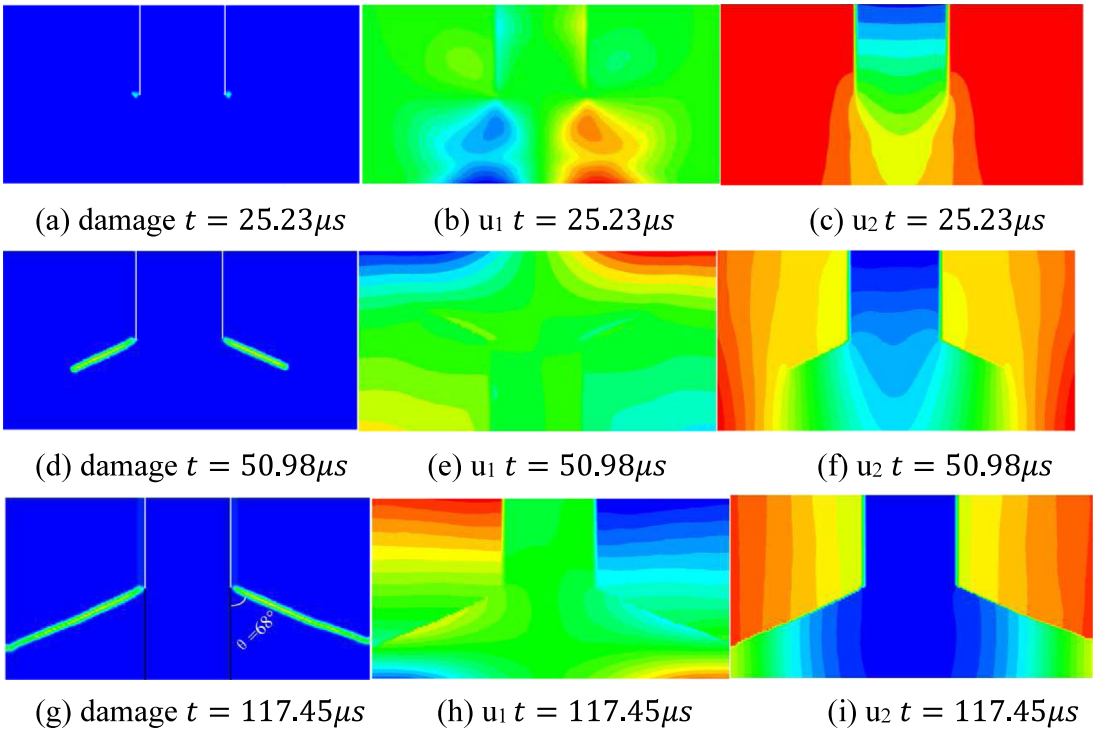

Fig. 26. The contour plots of the crack propagation at different time steps.

4. Conclusions

In this paper, a coupled method based on the boundary element method (BEM) and bond-based peridynamics (BBPD) is developed for modeling the dynamic crack propagation problems. The pre-crack and the potential propagation region are simulated by the BBPD dynamic equation, where the stiffness matrix is derived by the Taylor's expansion of the stretch. The rest of non-crack region is simulated by using the meshfree boundary-domain integral equation method to reduce the problem dimension by one, such that the computational efficiency

can be improved. A simple physical transform through the displacement continuity and force equilibrium at the interface nodes is employed to combine the two subregions for the global dynamic equation. This eliminates the need for overlapped elements or blending functions. The explicit and implicit time integral techniques can both be used to solve the coupled dynamic equations. However, the harmonic and transient dynamic numerical examples demonstrate that the implicit coupled BEM-PD methods are much easier to use and faster to deliver stable response results. The pre-cracked plate with traction and the Kalthoff–Winkler's example illustrate that the present coupled method can model the dynamic crack propagation accurately even with a coarse discretization. Because of the effectiveness and stability of the developed BEM-PD coupled method, it can be easily extended to model multiscale problems for which a large number of time steps in integration are required. Improved coupling schemes and extension to model crack propagation in 3D structures are possible topics for further work.

Declaration of competing interest

The authors declare that they have no known competing financial interests or personal relationships that could have appeared to influence the work reported in this paper.

Acknowledgments

The authors would like to thank the financial support from the National Natural Science Foundation of China (Project Nos. 11901283 and 11972179) and the Natural Science Basic Research Plan in Shaanxi Provincial of China (Project No. 2018JQ5079).

References

[1] E. Madenci, E. Oterkus, Peridynamic Theory and Its Applications, Springer, New York, 2014.
[2] S.A. Silling, Reformulation of elasticity theory for discontinuities and long-range forces, J. Mech. Phys. Solids 48 (1) (2000) 175–209.
[3] H. Zhang, X. Zhang, Y. Liu, P.Z. Qiao, Peridynamic modeling of elastic biomaterial interface fracture, Comput. Methods Appl. Mech. Engrg. 390 (2022) 114458.
[4] Y.X. Liu, L.S. Liu, H. Mei, Q.W. Liu, X. Lai, A modified rate-dependent peridynamic model with rotation effect for dynamic mechanical behavior of ceramic materials, Comput. Methods Appl. Mech. Engrg. 388 (2022) 114246.
[5] E. Madenci, A. Barut, M. Dorduncu, Peridynamic Differential Operator for Numerical Analysis, Springer, New York, 2019.
[6] Z.Q. Cheng, Z.B. Sui, H. Yin, H. Feng, Numerical simulation of dynamic fracture in functionally graded materials using peridynamic modeling with composite weighted bonds, Eng. Anal. Bound. Elem. 105 (2019) 31–46.
[7] A. Shojaei, T. Mudric, M. Zaccariotto, U. Galvanetto, A coupled meshless finite point/peridynamic method for 2D dynamic fracture analysis, Int. J. Mech. Sci. 119 (2016) 419–431.
[8] A. Shojaei, M. Zaccariotto, U. Galvanetto, Coupling of 2D discretized peridynamics with a meshless method based on classical elasticity using switching of nodal behaviour, Eng. Comput. 34 (5) (2017).
[9] R.W. Macek, S.A. Silling, Peridynamics via finite element analysis, Finite Elem. Anal. Des. 43 (15) (2007) 1169–1178.
[10] B. Kilic, E. Madenci, Coupling of peridynamic theory and the finite element method, J. Mech. Mater. Struct. 5 (2010) 707–733.
[11] W.Y. Liu, J.W. Hong, A coupling approach of discretized peridynamics with finite element method, Comput. Methods Appl. Mech. Engrg. 245–246 (2012) 163–175.
[12] G. Lubineau, Y. Azdoud, F. Han, C. Rey, A. Askari, A morphing strategy to couple non-local to local continuum mechanics, J. Mech. Phys. Solids 60 (6) (2012) 1088–1102.
[13] F. Han, G. Lubineau, Y. Azdoud, Adaptive coupling between damage mechanics and peridynamics: A route for objective simulation of material degradation up to complete failure, J. Mech. Phys. Solids 94 (2016) 453–472.
[14] U. Galvanetto, T. Mudric, A. Shojaei, M. Zaccariotto, An effective way to couple FEM meshes and peridynamics grids for the solution of static equilibrium problems, Mech. Res. Commun. 76 (2016) 41–47.
[15] M. Zaccariotto, D. Tomasi, U. Galvanetto, An enhanced coupling of PD grids to FE meshes, Mech. Res. Commun. (2017) S0093641317300824.
[16] M. Zaccariotto, T. Mudric, D. Tomasi, A. Shojaei, U. Galvanetto, et al., Coupling of FEM meshes with peridynamic grids, Comput. Methods Appl. Mech. Engrg. 330 (2018) 471–497.
[17] H. Li, H. Zhang, Y. Zheng, et al., An implicit coupling finite element and peridynamic method for dynamic problems of solid mechanics with crack propagation, Int. J. Appl. Mech. 10 (04) (2018) 1850037.
[18] Y. Bie, X. Cui, Z. Li, A coupling approach of state-based peridynamics with node-based smoothed finite element method, Comput. Methods Appl. Mech. Engrg. 331 (2018) 675–700.
[19] B. Sun, S. Li, Q. Gu, et al., Coupling of peridynamics and numerical substructure method for modeling structures with local discontinuities, Comput. Model. Eng. Sci. 120 (2019) 739–757.
[20] Y.J. Liu, Y.X. Li, W. Xie, Modeling of multiple crack propagation in 2-D elastic solids by the fast multipole boundary element method, Eng. Fract. Mech. 172 (2017) 1–16.

[21] Y.J. Liu, On the displacement discontinuity method and the boundary element method for solving 3-D crack problems, Eng. Fract. Mech. 164 (2016) 35–45.
[22] H. Wu, Y.J. Liu, W. Jiang, A fast multipole boundary element method for 3D multi-domain acoustic scattering problems based on the Burton–Miller formulation, Eng. Anal. Bound. Elem. 36 (5) (2012) 779–788.
[23] Y.J. Liu, Fast Multipole Boundary Element Method: Theory and Applications in Engineering, Cambridge University Press, Cambridge, 2009.
[24] Y. Yang, Y.J. Liu, Modeling of cracks in two-dimensional elastic bodies by coupling the boundary element method with peridynamics, Int. J. Solids Struct. 217–218 (2021) 74–89.
[25] S.A. Silling, Reformulation of elasticity theory for discontinuities and long-range forces, J. Mech. Phys. Solids 48 (1) (2000) 175–209.
[26] S.A. Silling, E. Askari, A meshfree method based on the peridynamic model of solid mechanics, Comput. Struct. 83 (2005) 1526–1535.
[27] D. Huang, G. Lu, C. Wang, et al., An extended peridynamic approach for deformation and fracture analysis, Eng. Fract. Mech. 141 (2015) 196–211.
[28] H. Yu, S. Li, On energy release rates in peridynamics, J. Mech. Phys. Solids 142 (2020) 104024.
[29] Y. Yang, C.C. Lam, K.P. Kou, Forced vibration analysis of functionally graded beams by the meshfree boundary-domain integral equation method, Eng. Anal. Bound. Elem. 72 (2016) 100–110.
[30] Y. Yang, K.P. Kou, V.P. Iu, C.C. Lam, C.Z. Zhang, Free vibration analysis of two-dimensional functionally graded structures by a meshfree boundary-domain integral equation method, Compos. Struct. 110 (2014) 342–353.
[31] D. Dipasquale, M. Zaccariotto, U. Galvanetto, Crack propagation with adaptive grid refinement in 2D peridynamics, Int. J. Fract. 190 (1–2) (2014) 1–22.
[32] Z. Cheng, G. Zhang, Y. Wang, B. Bobaru, A peridynamic model for dynamic fracture in functionally graded materials, Compos. Struct. 133 (2015) 529–546.
[33] G. Lu, D. Huang, P. Qiao, An improved peridynamic approach for quasi-static elastic deformation and brittle fracture analysis, Int. J. Mech. Sci. (2015).
[34] X. Kan, J. Yan, S. Li, et al., On differences and comparisons of peridynamic differential operators and nonlocal differential operators, Comput. Mech. 68 (6) (2021) 1349–1367.
[35] J.F. Kalthoff, S. Winkler, Failure mode transition at high rates of shear loading, DGM information's gesellschaft mbh, in: Impact Loading and Dynamic Behavior of Materials, Vol. 1, 1988, pp. 185–195.